Large-Eddy Simulation of Three-Dimensional Turbulent Free Surface Flow Past a Complex Stream Restoration Structure

Seokkoo Kang[1] and Fotis Sotiropoulos, M.ASCE[2]

Abstract: Large-eddy simulation (LES) of a three-dimensional, turbulent free surface flow past a stream restoration structure with arbitrarily complex geometries is presented. The three-dimensional, incompressible, spatially filtered Navier-Stokes and continuity equations are solved in generalized curvilinear coordinates. For the solution of mixed air-water flows, the curvilinear immersed boundary (CURVIB)–level set method developed previously is used and extended to carry out LES. Complex solid geometries are handled by the sharp-interface CURVIB method, and the subgrid scale stress terms arising from the spatial filtering of the Navier-Stokes equations are closed by the dynamic Smagorinsky model. To demonstrate the potential of the CURVIB–LES–level set model for simulating real-life, turbulent free surface flows involving arbitrarily complex geometries, LES is carried out for the flow past a complex rock structure that is fully submerged in water in a laboratory flume. The simulations show that the method is able to predict the time-averaged value as well as the root-mean-square fluctuations of water surfaces with good accuracy. Moreover, it is seen that the free surface flow at a high Froude number causes a significant level of fluctuations of water surface elevation and velocity at the water surface. **DOI: 10.1061/(ASCE)HY.1943-7900.0001034.**

Author keywords: Free surface flow; Level set method; Immersed boundary method; Large-eddy simulation; Turbulence.

Introduction

Free surface flows are often encountered in the practice of river and dam engineering, stream restoration, and coastal engineering. Predicting water elevation changes associated with a variety of flow phenomena occurring in the environment with good accuracy is an important prerequisite for the design of the engineering structures that are exposed continuously to water flows. Examples of such structures are groynes, vanes, drop structures, fish passages, weirs in rivers and streams, spillways, and coastal breakwaters, etc. Prediction of the large-scale water surface motions in the vicinity of complex structures has been a challenging undertaking because the dynamic motion of the air-water interface is fully coupled in a nonlinear manner with the instantaneous velocity and pressure fields. For that reason, the nonlinear three-dimensional (3D) free surface flow remains as one research area that has yet to be tackled.

Due to the nonlinearity and complexity of the free surface flow, solving the problem using analytic or mathematical models is almost impossible with a real-life free-surface flow with a high Reynolds number involving turbulence. To overcome such difficulties, numerical simulation has recently been used often for studying the free surface flows in the field of water resources and hydraulic engineering.

For the numerical modeling of free surface flows, several numerical modeling approaches with different levels of modeling sophistication exist. The simplest approach is solving one- (cross-sectional averaged) or two-dimensional (depth averaged) flow equations, which are called the shallow water equations (Yoon and Kang 2004). Depth-averaged models have been widely used in open-channel flow modeling because of their simplicity in treating the air-water interface and easy implementation. The drawback of the depth-averaged models, however, is that they are based on the assumptions that the pressure distribution in the vertical direction is hydrostatic, and that the vertical component of the flow acceleration is negligible. Moreover, they are not able to properly account for the influence of turbulence. For that reason, the applicability of depth-averaged models is inherently limited to relatively simple flows, and they are not adequate to tackle complex turbulent free surface flows.

A more advanced approach, which is capable of resolving 3D flows at the expense of sophisticated solution algorithms and higher computational cost, is the 3D numerical models solving the full Navier-Stokes equations. In these models, in addition to the Navier-Stokes equations, a separate free surface tracking equation is solved. Popular free surface tracking methods are arbitrary Lagrangian-Eulerian (ALE) methods and front-capturing methods. In ALE methods, the computational domain is discretized using a boundary-fitted curvilinear mesh that conforms with the instantaneous air-water interface at each time step. Usually, only the water part is solved in these methods, and the water surface elevation is assumed to be a single-valued function. In the front-capturing methods, on the other hand, the air and water domains are discretized using fixed-background grids within which the position of the interface is captured by an appropriate scalar marker function defined on the background grid. These methods have the advantage that the simultaneous simulation of the water and air phases is possible. Two important methods in this category are the volume-of-fluid (VOF) method of Hirt and Nichols (1981) and the level set method of Osher and Sethian (1988). The VOF method uses the marker function that is defined as the volume fraction of the water

[1]Assistant Professor, Dept. of Civil and Environmental Engineering, Hanyang Univ., Seoul 133-791, South Korea.

[2]Professor and Director, St. Anthony Falls Laboratory, Dept. of Civil Engineering, Univ. of Minnesota, 2 Third Ave. SE, Minneapolis, MN 55414 (corresponding author). E-mail: fotis@umn.edu

Note. This manuscript was submitted on June 19, 2014; approved on March 10, 2015; published online on June 1, 2015. Discussion period open until November 1, 2015; separate discussions must be submitted for individual papers. This paper is part of the ***Journal of Hydraulic Engineering***, © ASCE, ISSN 0733-9429/04015022(11)/$25.00.

in each grid cell. The level set method, on the other hand, uses the marker function that is defined as the distance from the closest liquid-gas interface. The marker function is zero at the interface, positive in the liquid phase, and negative in the gas phase. Only few studies have attempted to use the ALE, VOF, and level set methods to simulate 3D, viscous, free surface flows. Hodges and Street (1999), for instance, simulated finite-amplitude surface waves over a flat bed using an ALE method in conjunction with a boundary-orthogonal curvilinear grid. Ramamurthy et al. (2007) used VOF methods in conjunction with the Reynolds-averaged Navier-Stokes (RANS) turbulence modeling to simulate 3D free surface flow. Kara et al. (2014) used the level set method along with large-eddy simulation (LES) to simulate the flow through a submerged bridge-opening structure. Yue et al. (2005) solved free surface flow over a laboratory-scale, simple-shaped dune using the LES with the level set method. Kang and Sotiropoulos (2012b), on the other hand, simulated the turbulent free surface flow past a submerged hydraulic structure and that in a field-scale sinuous meandering channel using the level set method with the curvilinear immersed boundary (CURVIB) method and a RANS turbulence closure model. To the best of the authors' knowledge, the work of Kang and Sotiropoulos (2012b) is the only study that has tackled real-life free surface flow problems involving turbulence and arbitrarily complex geometries. However, these RANS model–based free surface solvers have the disadvantage that they cannot account for water surface fluctuations due to turbulence, which could be important at high-Froude-number flows. For instance, in the hydraulic jump roller, it is known that large vertical fluctuations of the free surface elevation due to turbulence are observed (Chachereau and Chanson 2011). In such cases, it would be of great importance to account for the temporal water surface fluctuations in the numerical modeling.

With the development of high-performance supercomputers and advanced computing algorithms during the last decade, LES has been gradually replacing RANS modeling for computing turbulent flows and has now emerged as a powerful tool for solving complex flow phenomena encountered in a broad range of science and engineering, which include wind farm simulation (Yang et al. 2012), modeling of flow around wind and hydrokinetic turbines (Kang et al. 2012), and simulation of turbulent flows in rivers (Kang et al. 2011; Kang and Sotiropoulos 2011, 2012a). One area that has yet to be tackled by LES is the prediction of free surface flows occurring in rivers and oceans. An important characteristic of the LES in comparison to the RANS model is that the LES is able to resolve instantaneous coherent flow structures whose size is larger than the local filter size. Thus, LES, when coupled with an appropriate free surface flow model, is able to resolve the instantaneous fluctuation of the velocity field as well as the water surface.

The objective of this study is to develop a versatile numerical model for carrying out LES of free surface flow past arbitrarily complex real-life in-stream structures in open channels. To that end, a coupled LES–level set method is developed in conjunction with the CURVIB method, which is ideal for handling arbitrarily complex geometries existing in natural streams. The predictive capabilities of the developed model is verified by applying it to simulate the turbulent free surface flow past a complex stream restoration structure. The computed results are compared with the measured mean water surface elevations and the root-mean-square water surface fluctuations. LES of a high-Froude-number flow is also carried out for the same stream restoration structure, and the characteristics of the water surface deformation in relation to turbulence are discussed.

The paper presents the governing equations for two-phase, free surface flow. Next, the numerical method is developed for solving them. The CURVIB–LES–level set method is applied to simulate turbulent free surface flow in a straight laboratory flume with an embedded stream restoration structure. The predictive capabilities and the applicability of the numerical model for complex free surface flows are demonstrated. Finally, the findings are summarized and the conclusions of this study are presented.

Governing Equations for Two-Phase Free Surface Flow

Filtered Navier-Stokes Equations

The governing equations are the 3D spatially filtered Navier-Stokes equations for two immiscible and incompressible fluids formulated using the level set approach (Osher and Sethian 1988). The governing equations are first formulated in Cartesian coordinates $\{x_i\}$ (where $i = 1, 2, 3$) and then transformed fully (both the velocity vector and spatial coordinates are expressed in curvilinear coordinates) in generalized, curvilinear coordinates $\{\xi^i\}$ as required by the CURVIB method (Ge and Sotiropoulos 2007; Kang et al. 2011). This section presents the resulting equations in compact tensor notation (repeated indices imply summation).

Let ϕ denote the spatially filtered level set function, which measures the distance to the closest fluid interface and is positive in the water region, negative in the air region, and zero at the interface. Then, the two-fluid, level set form of the spatially filtered continuity and Navier-Stokes equations reads as follows ($i,j = 1, 2, 3$):

$$J\frac{\partial U^j}{\partial \xi^j} = 0 \tag{1}$$

$$\frac{1}{J}\frac{\partial U^i}{\partial t} = \frac{\xi_l^i}{J}\left\{-\frac{\partial}{\partial \xi^j}(U^j u_l) + \frac{1}{\rho(\phi)}\frac{\partial}{\partial \xi^j}\left[\mu(\phi)\frac{g^{jk}}{J}\frac{\partial u_l}{\partial \xi^k}\right] - \frac{1}{\rho(\phi)}\frac{\partial}{\partial \xi^j}\left(\frac{\xi_l^j p}{J}\right) - \frac{1}{\rho(\phi)}\frac{\partial \tau_{lj}}{\partial \xi^j} + G_i\right\} \tag{2}$$

where $\xi_l^i = \partial \xi^i / \partial x_l$ = the transformation metrics; J = Jacobian of the geometric transformation; u_i = the ith component of the spatially filtered velocity vector in Cartesian coordinates; $U^i = (\xi_m^i / J)u_m$ = filtered contravariant volume flux; $g^{jk} = \xi_l^j \xi_l^k$ = components of the contravariant metric tensor; ρ = density; μ = dynamic viscosity; p = pressure; τ_{ij} = subgrid scale (SGS) stress tensor; and G_i = acceleration vector due to gravity.

For a two-fluid formulation, the density and viscosity of the fluid vary as a function of ϕ, transitioning smoothly across the interface from the respective values in the water phase to those in the air phase, as follows:

$$\rho(\phi) = \rho_{\text{air}} + (\rho_{\text{water}} - \rho_{\text{air}})h(\phi) \tag{3}$$

$$\mu(\phi) = \mu_{\text{air}} + (\mu_{\text{water}} - \mu_{\text{air}})h(\phi) \tag{4}$$

where $h(\phi)$ = the smoothed Heaviside function given as follows:

$$h(\phi) = \begin{cases} 0 & \phi < -\epsilon, \\ \frac{1}{2} + \frac{\phi}{2\epsilon} + \frac{1}{2\pi}\sin\left(\frac{\pi\phi}{\epsilon}\right) & -\epsilon \le \phi \le \epsilon \\ 1 & \epsilon < \phi, \end{cases} \tag{5}$$

where ϵ = a tunable parameter that determines the thickness of the numerical smearing of the interface (Osher and Fedkiw 2002). The value of ϵ is usually set to be equal to the length of one to two grid spacings. The smoothing of the interface achieved by introducing

J. Hydraul. Eng. 2015.141.

the Heaviside function renders the density, velocity, and pressure fields continuous across the interface and prevents potential numerical instabilities.

The SGS stress tensor, τ_{ij}, in Eq. (2) is modeled using the Smagorinsky model (Smagorinsky 1963) as follows:

$$\tau_{ij} = -2\mu_t S_{ij} \tag{6}$$

where S_{ij} = filtered strain-rate tensor; μ_t = dynamic eddy viscosity; and δ_{ij} = Kronecker delta. The eddy viscosity is calculated by solving the dynamic Smagorinsky SGS model (Germano et al. 1991).

Level Set Equations

The governing equation for ϕ, which represents the motion of the interface of two immiscible fluids (e.g., air and water), in curvilinear grids is written as

$$\frac{1}{J}\frac{\partial \phi}{\partial t} + U^j \frac{\partial \phi}{\partial \xi^j} = -\left\langle U^{j'}, \frac{\partial \phi'}{\partial \xi^j} \right\rangle \tag{7}$$

where $\langle\,\rangle$ and the superscript $'$ = spatial filtering operation and spatial fluctuation, respectively. Due to the spatial filtering of the nonlinear term associated with ϕ and U, a second-order correlation term involving instantaneous fluctuations of ϕ and U^j appears on the right-hand side of Eq. (7). In the authors' model, the term on the right-hand side of the equation has been neglected assuming, in the present application, that the correlation between the gradient of the spatial fluctuations of the level set function and the contravariant volume flux is negligible. In the multiphase flow where there exists strong mixing between fluids at different phases (e.g., oil spill in the ocean), the contribution of these terms may be significant.

Generally, the level set function computed by solving Eq. (7) does not satisfy the distance function requirement, which is $|\nabla\phi| = 1$, especially in the region away from the gas/liquid interface. If the distance function is not preserved, the gradient of ϕ can become large and leads to a loss of accuracy; thus, keeping the level set function as a distance function, at least within the several grid cells near the interface, is very important in the level set method. To preserve the distance function, Sussman et al. (1994) suggested solving the following reinitialization equation:

$$\frac{\partial \phi}{\partial \tau} + S(\phi_0)(|\nabla\phi| - 1) = 0 \tag{8}$$

where $\partial()/\partial\tau$ = pseudo-time derivative, which is driven to zero during every physical time step through iterations; ϕ_0 = level set function at the beginning of the pseudo-time iteration; and S = smoothed sign function given by

$$S(\phi_0) = \begin{cases} 1 & \phi_0 \geq \epsilon, \\ -1 & \phi_0 \leq -\epsilon, \\ \dfrac{\phi_0}{\epsilon} - \dfrac{1}{\pi}\sin\left(\dfrac{\pi\phi_0}{\epsilon}\right) & \text{otherwise} \end{cases} \tag{9}$$

Although the solutions of Eqs. (7) and (8) satisfy the distance function requirement, they do not guarantee conservation of mass. Because this can lead to loss or gain of air/water volume, one needs to solve the mass conserving reinitialization equation proposed by Sussman and Fatemi (1999), which adds the mass correction term to the right-hand side of Eq. (8) as follows:

$$\frac{\partial \phi}{\partial \tau} + S(\phi_0)(|\nabla\phi| - 1) = \lambda\tilde{\delta}(\phi)|\nabla\phi| \tag{10}$$

with

$$\lambda = -\frac{\int_\Omega \tilde{\delta}(\phi)S(\phi_o)1 - |\nabla\phi|d\Omega}{\int_\Omega \tilde{\delta}^2(\phi)\nabla\phi|d\Omega} \tag{11}$$

where Ω = volume of an individual grid cell. The value of λ is constant within each grid cell.

Numerical Methods

Numerical Methods for Solving Governing Equations

The numerical method for solving the coupled Navier-Stokes and level set equations in the generalized curvilinear coordinates was developed by Kang and Sotiropoulos (2012b). They extended the hybrid staggered/nonstaggered grid fractional step method proposed by Ge and Sotiropoulos (2007) to multiphase flow simulation. The methods for solving Navier-Stokes and level set equations developed in Kang and Sotiropoulos (2012b) are also used in this study. For instance, the level set equation for the interface motion [Eq. (7)] is discretized in space by the third-order weighted essentially non-oscillatory (WENO) scheme (Jiang and Shu 1996), and the discrete equation is advanced in time using the second-order Runge-Kutta method. The gradient term in the mass conserving reinitialization equation [Eq. (10)] is discretized by the second-order essentially non-oscillatory (ENO) scheme proposed by Sussman et al. (1998).

Because the numerical diffusion arising from the discretization of the Navier-Stokes equations needs to be minimized in LES, the three-point second-order central differencing is used for the discretization of the advection term of the Navier-Stokes equations instead of the third-order WENO scheme, which was used in a previous study (Kang and Sotiropoulos 2012b) for RANS simulations.

The accuracy of the free surface flow solution algorithms has already been well verified in Kang and Sotiropoulos (2012b) by solving free surface flows with analytic solutions, and no additional quantitative verification of numerical accuracy is carried out. For more details of the numerical methods and validation of the model, readers are referred to Kang and Sotiropoulos (2012b).

Handling Complex Geometries

An important prerequisite of a numerical model for simulating real-life flow phenomena is to be able to handle arbitrarily complex geometries. To that end, CURVIB method is used (Ge and Sotiropoulos 2007). In the CURVIB method, the geometries of the complex in-stream structures are discretized with an unstructured triangular mesh and embedded in a background curvilinear grid used to discretize a channel of regular cross section that fully contains the streambed bathymetry. The grid nodes of the curvilinear mesh are classified as follows based on their location relative to the immersed streambed bathymetry: nodes exterior to the flow domain, which are blanked out of the computation; interior (or fluid) nodes where the governing equations are solved; and immersed boundary (IB) nodes, which are located in the fluid domain but in the immediate vicinity of the immersed boundary. Boundary conditions for the velocity components at the IB nodes are specified using a reconstruction approach. When the grid is fine enough to resolve the near-wall viscous layer, linear or quadratic interpolation along the local normal to the boundary directions

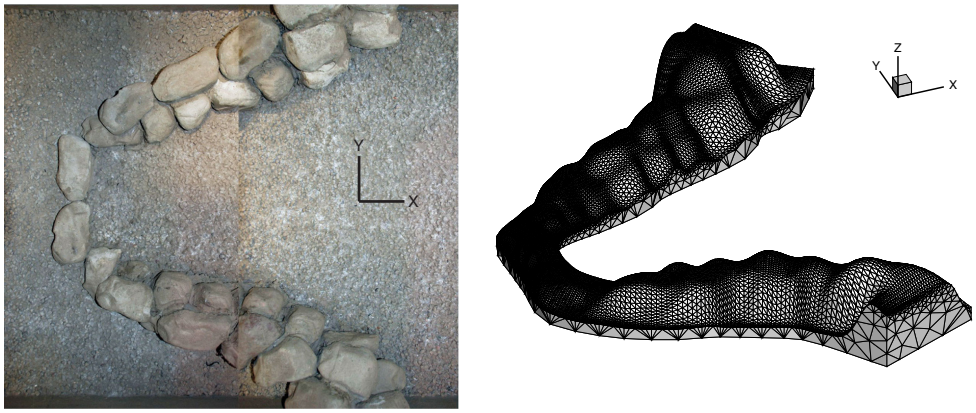

Fig. 1. (a) Cross vane used in the laboratory experiment (photo by Seokkoo Kang); (b) immersed boundary mesh reconstructed from the measured topography

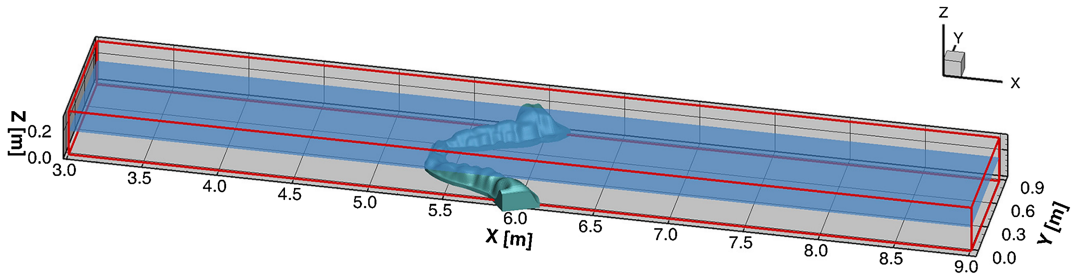

Fig. 2. Computational domain and the initial water surface

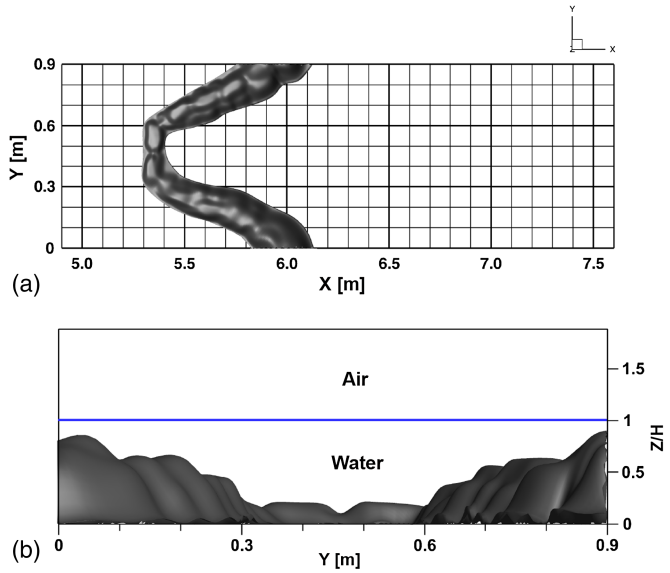

Fig. 3. A schematic showing the position of the cross vane in a computational domain: (a) top view; (b) front view; H is the mean downstream water surface elevation

(Ge and Sotiropoulos 2007; Kang et al. 2011) is used. On the other hand, when the IB nodes are located in the logarithmic layer, a wall model (Kang et al. 2011) is used.

The CURVIB method has been successfully applied to simulate a wide range of complex flows. The method has recently

Table 1. Details of the Computational Grids Used in the LES

Grid parameters	LES-1	LES-2
$N_x \times N_y \times N_z$	$151 \times 94 \times 307$	$219 \times 114 \times 444$
Number of nodes	4.36×10^6	1.11×10^7
Δx^+	50–1,800	75–3,000
Δy^+	30–200	45–150
Δz^+	30–200	45–138

Note: Δx^+, Δy^+, Δz^+ and N_x, N_y, N_z indicate the grid spacing in wall units and the number of grid nodes in the x, y, z directions, respectively.

Table 2. Summary of the Flow Parameters of LES-1 and LES-2

Flow parameters	LES-1	LES-2
μ_a (dynamic viscosity of air)	1.78×10^{-5} kg/(m · s)	1.78×10^{-5} kg/(m · s)
μ_w (dynamic viscosity of water)	10^{-3} kg/(m · s)	10^{-3} kg/(m · s)
ρ_a (air density)	1.2 kg/m^3	1.2 kg/m^3
ρ_w (water density)	1,000 kg/m^3	1,000 kg/m^3
B (channel width)	0.90 m	0.90 m
H (downstream flow depth)	0.17 m	0.17 m
Q (flow discharge)	3.81×10^{-2} m^3/s	7.62×10^{-2} m^3/s
$U_0(=Q/BH)$	0.25 m/s	0.50 m/s
u_τ (mean friction velocity)	0.02 m/s	0.03 m/s
$R(=U_0H/\nu_w)$	4.23×10^4	8.46×10^4
$F(=U_0/\sqrt{gH})$	0.19	0.39

been applied to solve turbulent flows through natural river reaches (Kang et al. 2011; Kang and Sotiropoulos 2011, 2012a), to simulate sediment transport and scour phenomena in open channels with embedded hydraulic structures (Khosronejad et al. 2011, 2012), and to simulate turbulent flows in a wind farm and around hydrokinetic turbines (Yang et al. 2012; Kang et al. 2012, 2014).

Simulation of Flow Past a Cross Vane

Turbulent flow in a straight open channel is considered with the embedded rock structure seen in Fig. 1(a). This structure is a cross vane that is widely used in stream restoration projects for mitigating streambank erosion (Rosgen 2001). In a previous study (Kang and Sotiropoulos 2012b), the same cross-vane structure was used to validate the RANS–level set free surface model. This is a good test case that can be used for demonstrating the capability of the model for predicting turbulent free surface flows and handling complex geometries.

LES were carried out for the two different cases. In the first LES (LES-1), the discharge and the far downstream flow depth are $Q = 3.81 \times 10^{-2}$ m^3/s and $H = 0.17$ m. In the second LES (LES-2), Q is increased to twice as large as that of the LES-1 ($Q = 7.62 \times 10^{-2}$ m^3/s) while the downstream flow depth remains the same.

A laboratory experiment was carried out for LES-1. Because the details of the laboratory experiment are explained in Kang and Sotiropoulos (2012b), a brief summary is presented here. The experiment was carried out in a flume at St. Anthony Falls Laboratory (SAFL), which is 0.9 m wide and 12 m long. The mean water surface profile and root-mean-square (RMS) value of water surface fluctuations at several measurement locations were collected using an ultrasonic distance sensor. The cross vane is installed at 6 m downstream from the inlet of the flume. The mean flow discharge (Q)

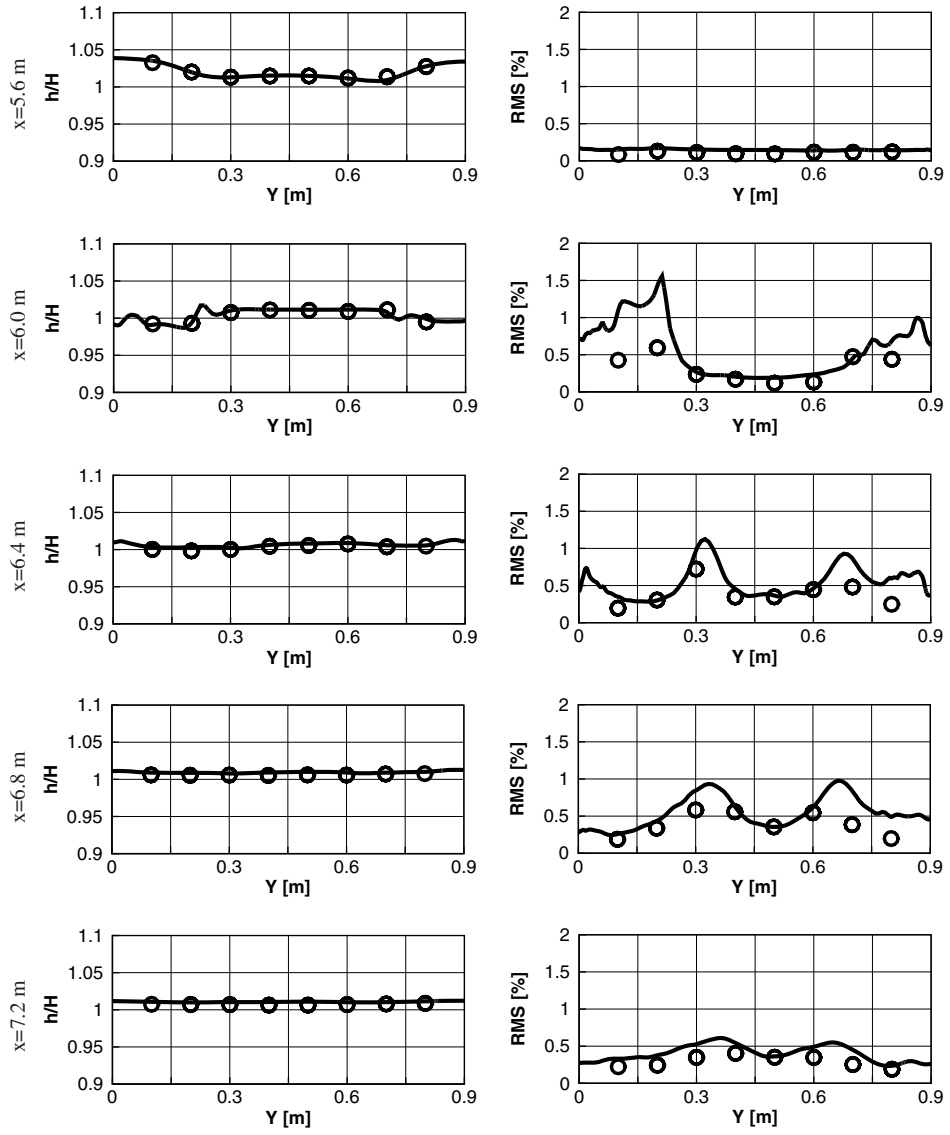

Fig. 4. Comparison of the computed and measured time-averaged water surface elevation (h) and the RMS of the water surface fluctuation nondimensionalized by the mean downstream water surface elevation (H); lines and symbols indicate the LES and measurements, respectively

is 3.81×10^{-2} m^3/s, which corresponds to a Reynolds number of 4.23×10^4 and a Froude number of 0.19 based on the downstream flow depth ($H = 0.17$ m) and the mean flow velocity ($U_0 = 0.25$ m/s). The 3D topography of the cross vane in the flume was scanned using the high-resolution laser topography scanner at submillimeter resolution, and it was used to reconstruct the immersed boundary mesh [Figs. 1(b), 2, and 3] for the numerical simulation. As seen in Fig. 3, shallow-depth regions exist near the sidewalls, where the cross-vane structure is mounted. The local flow depth in these regions is approximately 10% of the mean flow depth (H).

The schematic describing the computational domain used in the LES is shown in Fig. 2, and the position of the cross vane is shown in detail in Fig. 3. The inlet and outlet of the computational domain are located at $x = 3$ m and $x = 9$ m, respectively. In Tables 1 and 2, the details of the computational grids and flow parameters, respectively, for LES-1 and LES-2 are summarized. In LES-1, the grid spacing in the x, y, and z directions in wall units is in the range of approximately 9–300, 5–30, and 5–30, respectively. In the region where the first off-wall node in the vicinity of the solid boundary is outside the logarithmic layer, a wall modeling approach (Kang et al. 2011) is used. As seen in Fig. 2, the cross-vane geometry obtained from the topography scanner was converted to the immersed boundary mesh and is located at approximately $x = 6$ m in the computational domain.

LES-1: Baseline Case

This section presents the computed flow field of the LES-1 case and compares the computed water surfaces with the measurements.

In Fig. 4, the profiles of the time-averaged mean and RMS water surface fluctuation at $x = 5.6$, 6, 6.4, 6.8, and 7.2 m are compared. As seen, the computed mean water depth profiles are in very good agreement with the measurement. Moreover, the LES reproduces the measured RMS fluctuation profiles with good accuracy. Although the RMS value is overpredicted in the region close to the $y = 0$ sidewall at the $x = 6$ m cross section, the overall comparisons in other regions are satisfactory. The discrepancy seen at $x = 6$ m could be attributed to the uncertainties of the numerical simulation due to the fact that the LES could not fully resolve the rock geometries of the cross vane. For instance, empty space exists between the rocks that comprise the cross vane, but in the reconstructed immersed boundary mesh [Fig. 1(b)], the empty space could not be resolved with sufficient accuracy because the spacing of the background is coarser than the gap size. Nevertheless, the overall good agreement is seen in the present LES and demonstrates the predictive capabilities of the coupled CURVIB–LES–level set method for turbulent free surface flows around a submerged highly complex hydraulic structure.

In Fig. 5, the contours of the instantaneous downstream velocity and water surface elevation are plotted. As seen, the cross vane creates low-velocity zones near the sidewalls and the high-velocity region at the center region of the channel. It is also seen that water surface ripples emanating from the sidewalls are formed and are directed toward the channel center in the instantaneous flow depth contours [Fig. 5(b)].

In Fig. 6, the computed mean downstream velocity, the mean flow depth, the RMS fluctuation of the flow depth, and the local Froude number are plotted. The water depth increase due to the backwater effect in the upstream region is approximately 3–4% of the mean flow depth. The water surface ripples are also clearly visible in the mean flow depth contours. It is interesting to observe in the velocity contours that high- and low-velocity regions are formed in the troughs and crests of the wavy water surfaces, respectively. The mean velocity field also shows the presence of shear layers separating the center-region high-velocity core and the near-sidewall low-velocity regions. Moreover, the RMS water surface fluctuation contours show that higher water surface fluctuations are seen along the region of the shear layers. The magnitude of the RMS fluctuation along the shear layer regions is approximately 0.5% relative to the mean flow depth (H). The high water surface fluctuation is the result of the velocity fluctuation due to the turbulence generated along the shear layer. The local Froude number contours are also plotted [Fig. 6(d)]. The local Froude number is defined as $\langle \bar{V} \rangle / \sqrt{g\langle h \rangle}$, where V is the instantaneous velocity magnitude, and $\langle \cdot \rangle$ and the overbar indicate time-averaging and depth-averaging $[(1/h)\int_0^h (\cdot) dz]$ operations, respectively. It is seen in the figure that, near the sidewalls of the channel and where the flow depth is shallow, there is a region of supercritical flows where the Froude number exceeds 1, which implies that a small hydraulic jump occurs due to a very shallow water depth.

Fig. 7 plots the contours of the velocity variances, $\overline{u'u'}$, $\overline{v'v'}$, and $\overline{w'w'}$, at the water surface. The overbar indicates the time-averaging operation. It is observed that high levels of x and y velocity fluctuations are observed along the position of the shear layers in the center region. Moreover, the $\overline{w'w'}$ contour indicates that the overall magnitude of the velocity fluctuation in the vertical (z) direction is significantly lower than that in other directions. However, in the shallow-depth regions near the sidewalls where the rock structures are attached, the magnitude of $\overline{w'w'}$ is comparable to that of $\overline{u'u'}$ and $\overline{v'v'}$. This suggests that, in these regions, the vertical component of the velocity fluctuation, which is also related to the water surface fluctuation, is significant. A similar trend is also observed in the water surface RMS contours [Fig. 6(c)].

This section carries out LES of the free surface flow past a complex submerged hydraulic structure. It is demonstrated that

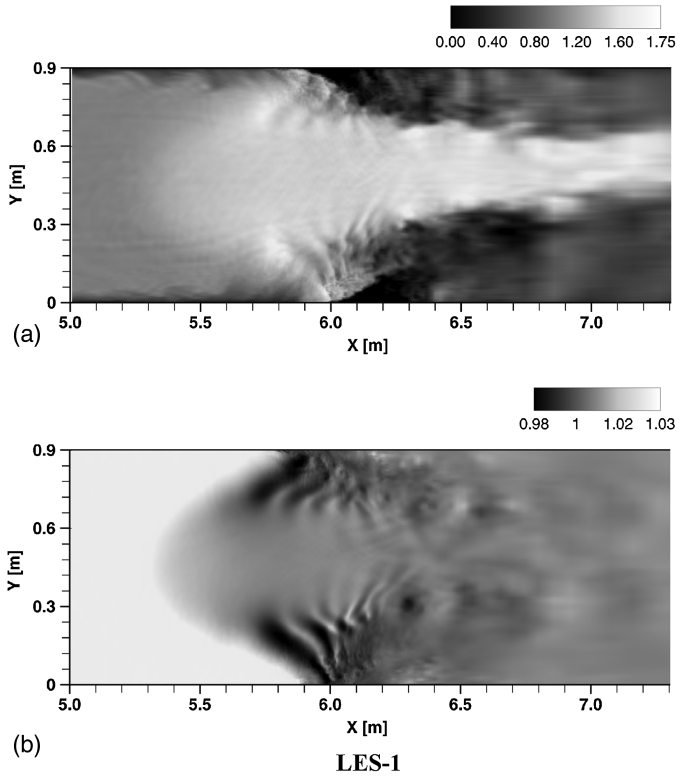

Fig. 5. Plan view of the contours of the computed instantaneous flow field on the water surface (LES-1): (a) the dimensionless downstream velocity (u/U_0); (b) the dimensionless flow depth (h/H)

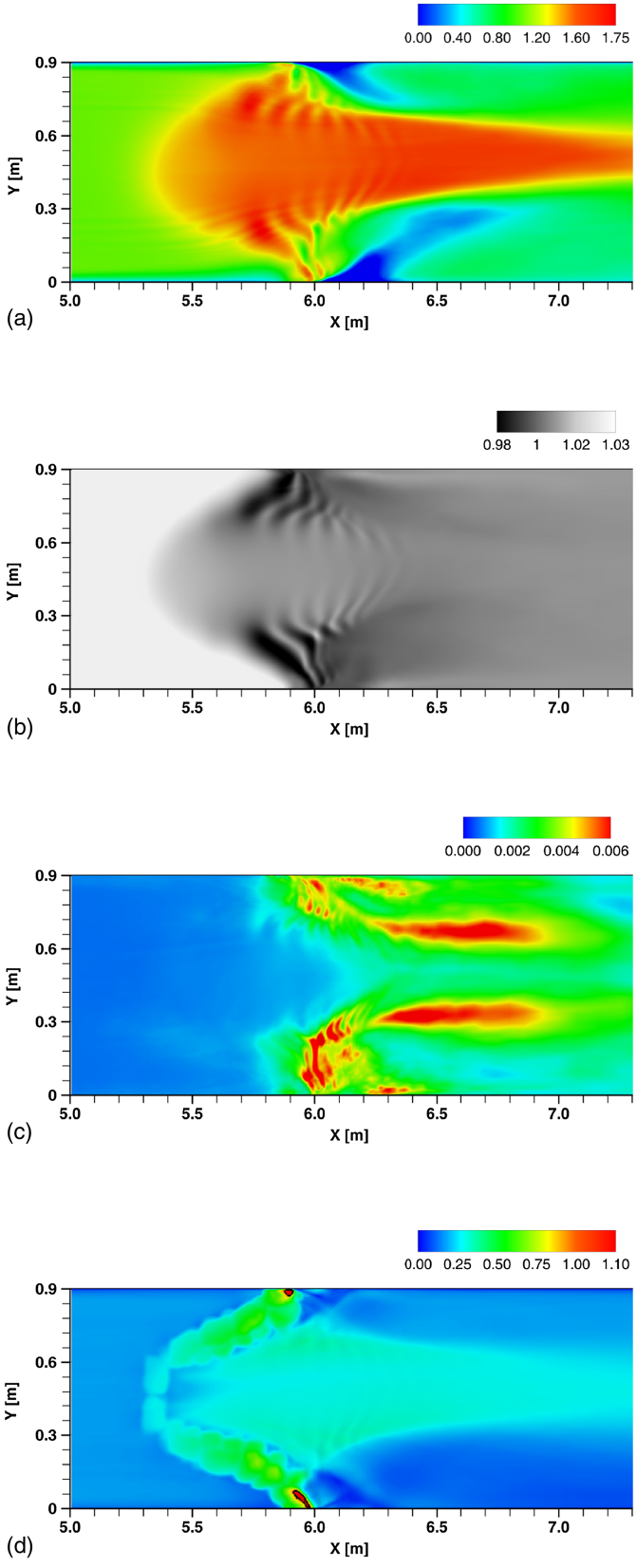

LES-1 (Lower discharge)

Fig. 6. Plan view of the contours of the computed mean flow field on the water surface (LES-1): (a) the dimensionless downstream velocity ($\langle u \rangle / U_0$); (b) the dimensionless flow depth ($\langle h \rangle / H$); (c) the dimensionless RMS fluctuation of the water depth (h_{rms}/H); (d) the local Froude number; the solid lines in Fig. 6(d) mark the contours of the Froude number equal to 1

the numerical model is capable of predicting the mean free surface elevation as well as the RMS fluctuation with good accuracy. The next section will carry out LES for the same structure at a higher discharge.

LES-2: Higher Flow Case

The previous section showed that the mean water surfaces and the RMS water surface fluctuations predicted by the LES agree well with the measurements both qualitatively and quantitatively. This suggests that the LES-predicted water surface fluctuations, such as those associated with the instantaneous water surface ripples [Fig. 5(b)] emanating from the crest of the rock structure attached to the sidewalls, where a local Froude number exceeds 1 and a hydraulic jump occurs [Fig. 6(d)], are not numerical artifacts but physical phenomena. One can easily expect that such effects would become more significant especially at higher Reynolds numbers because the water surface fluctuation is strongly linked to the vertical velocity fluctuations (or vertical turbulence intensity).

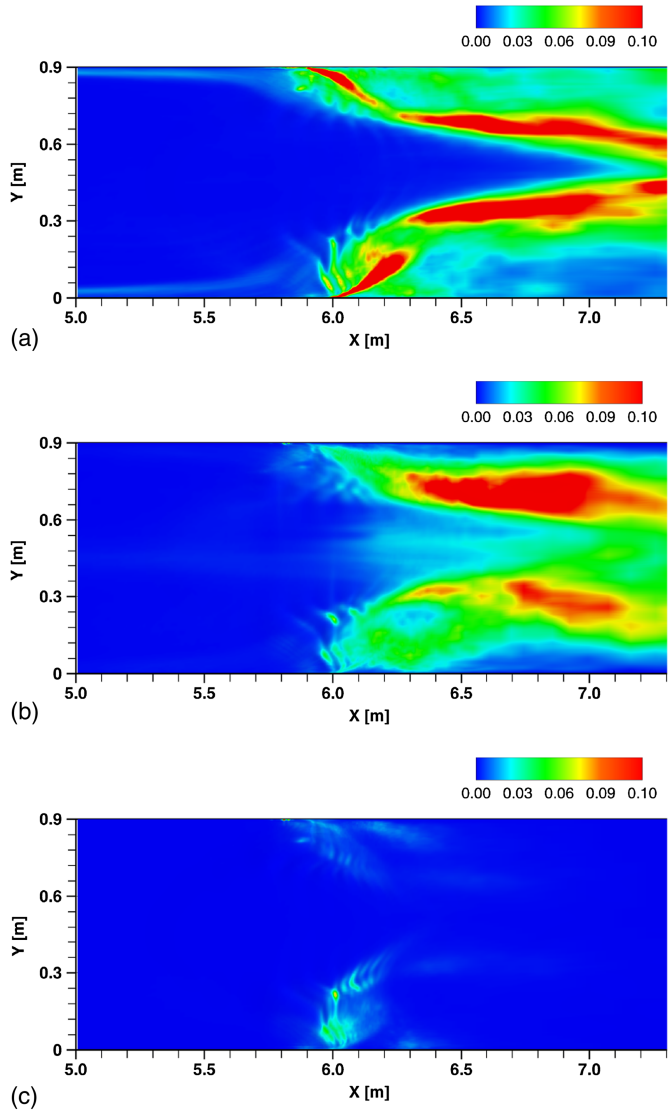

LES-1 (Q=3.81×10^{-2} m^3/s)

Fig. 7. Plan view of time-averaged velocity variances at the water surface nondimensionalized by U_0^2 (LES-1): (a) streamwise (x-direction); (b) spanwise (y-direction); and (c) vertical (z-direction) velocity variances

To investigate this issue, a numerical experiment is carried out to assess how the increase in Reynolds number influences the water surface fluctuations. Specifically, LES of the free surface flow past the same structure as that considered in the previous section with a higher discharge is carried out. The goal of this LES is to demonstrate the applicability of the present numerical model for simulating 3D free surface flows with larger free surface deformation. This discharge in the present case ($Q = 7.62 \times 10^{-2}$ m^3/s) is increased by twice that of LES-1. All other boundary conditions are kept the same as LES-1.

In Figs. 8 and 9, the contours of the instantaneous and mean flow field are plotted, respectively. As seen, they exhibit flow patterns that are largely different from those of LES-1. Fig. 8 shows that the width of the high-velocity core is significantly increased compared to LES-1. It is also observed that instantaneous water surface elevations in LES-2 exhibit a much higher level of complexity in comparison to LES-1 [Fig. 5(b)]. An interesting observation is that there exists a sudden change in water surface elevation and the downstream velocity across the shallow-depth regions directly above the crest of the cross vane near the channel sidewalls. This phenomenon is presumably related to the formation of a hydraulic jump across the crest of the cross vane, where the Froude number locally exceeds 1 due to the shallow depth and a relatively high approach flow speed. Fig. 10 shows a 3D view of the computed instantaneous water surfaces over the rock structure. Wavy water surfaces in the wake of the rock structure are clearly seen in the figure. One can also observe that highly complex water surface motions emanating from the channel sidewalls characterized by small-scale water ripples are captured by the present numerical model.

The mean flow field in Fig. 9, on the other hand, shows that the small-scale water surface ripples observed in LES-1 are not seen in

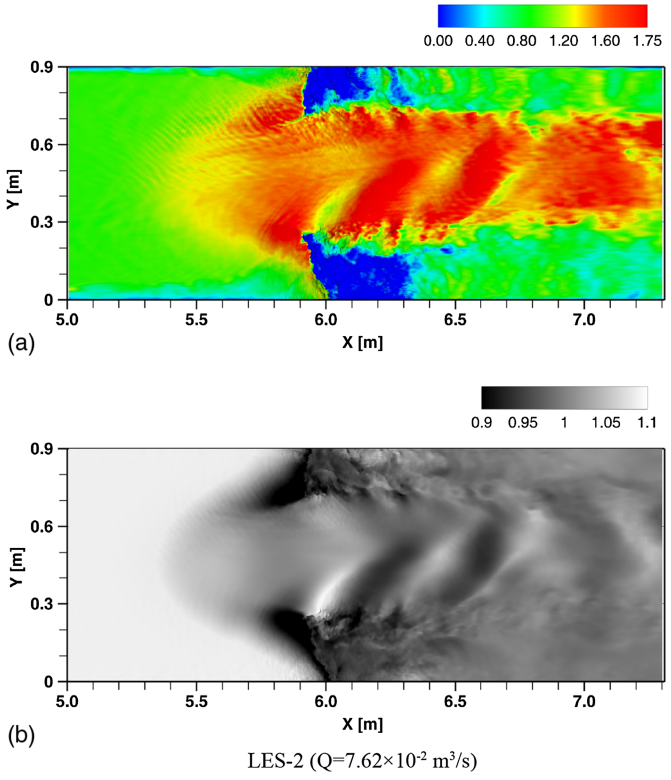

Fig. 8. Plan view of the contours of the computed instantaneous flow field on the water surface (LES-2): (a) the dimensionless downstream velocity ($\langle u \rangle / U_0$); (b) the dimensionless flow depth (h/H)

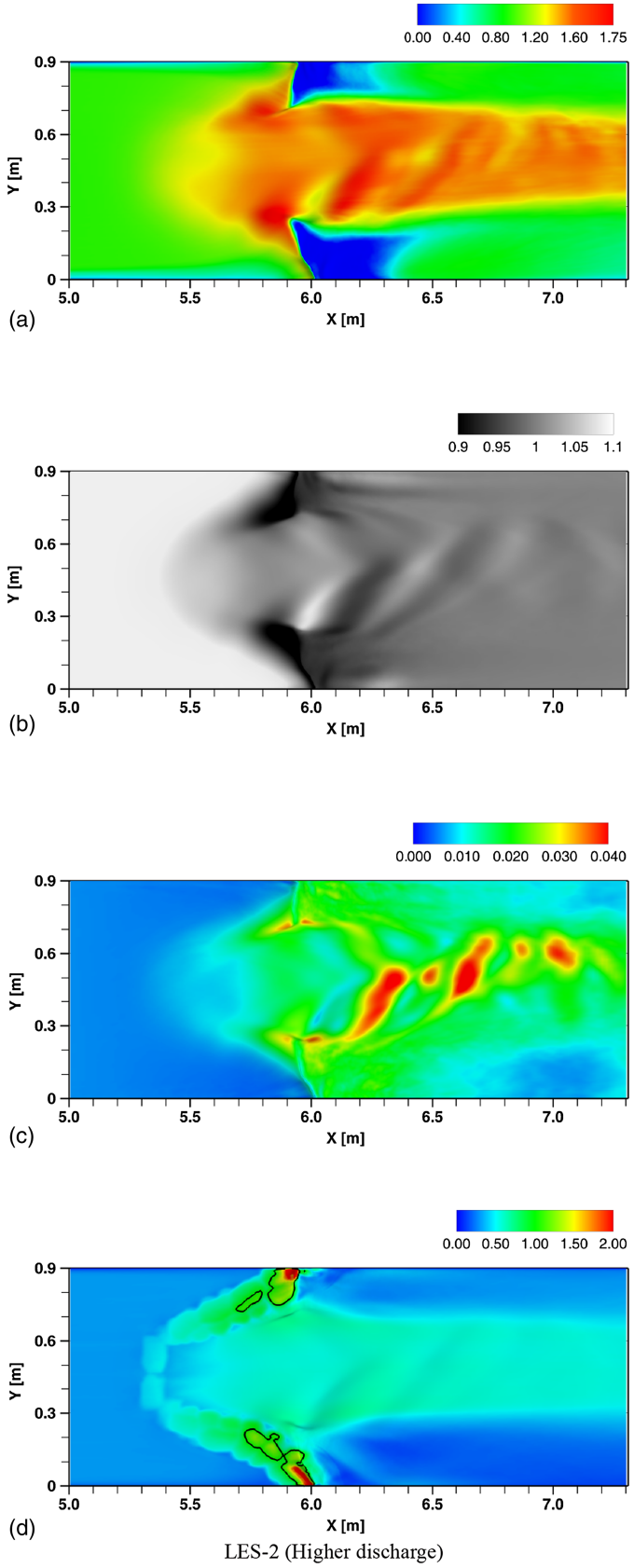

Fig. 9. Plan view of the contours of the computed mean flow field on the water surface (LES-2): (a) the dimensionless downstream velocity ($\langle u \rangle / U_0$); (b) the dimensionless RMS fluctuation of the water depth ($\langle h \rangle / H$); (c) the dimensionless RMS fluctuation of the water depth (h_{rms}/H); (d) the local Froude number; the solid lines in Fig. 9(d) mark the contours of the Froude number equal to 1

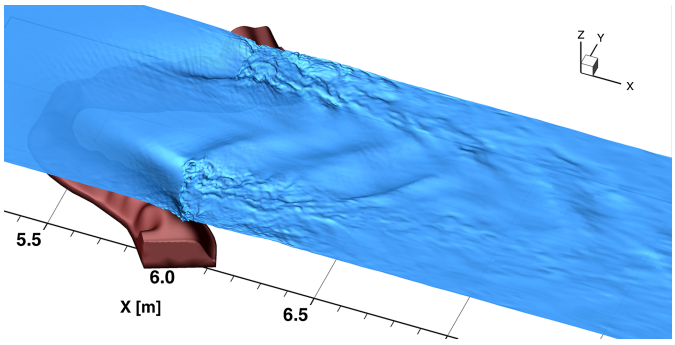

Fig. 10. Three-dimensional view of the computed instantaneous water surfaces over the rock structure (LES-2)

LES-2. Instead, a large-scale free surface deformation is seen along the center region of the channel. The computed minimum and maximum free surface deformations are approximately 15% relative to the mean downstream water depth (H), respectively. Moreover, the maximum RMS value in this case amounts to approximately 5% of the mean flow depth. It is almost an order of magnitude larger the value of LES-1, which suggests that, at a high-Froude-number flow, the free surface deformation in the vicinity of a submerged structure is no longer negligible. To further investigate the existence of a hydraulic jump above the rock structure, the longitudinal profiles of the time-averaged dimensionless flow depth, bed elevation, and the local Froude number are plotted in Fig. 11. It is clearly seen in the figure that the regions of supercritical flows exist where the local Froude number exceeds 1 in both LES-1 and LES-2, and particularly at $y/B = 0.05$, it is observed that the peak Froude number is larger than 2 in LES-2. The comparison of the water surface and Froude number profiles shows that the location where a sudden rise of water surface occurs coincides approximately with the location where the local Froude number is approximately 1. This confirms the existence of small-scale hydraulic jumps seen in the instantaneous and mean flow fields.

Fig. 12 plots the contours of the velocity variances, $\overline{u'u'}$, $\overline{v'v'}$, and $\overline{w'w'}$, at the water surface. The contours indicate that, along the shear layers, a high level of turbulence intensity is observed with much larger magnitudes compared to LES-1. It is worth mentioning that the magnitude of $\overline{w'w'}$ in the shear layer region is comparable to that of the other components, which means the free surface fluctuation contributes significantly to the generation of velocity fluctuation in the vertical direction. Furthermore, pockets of high levels of turbulence intensity are observed in the region where the sudden change in velocity and water surface elevation was observed. The magnitude of the dimensionless velocity

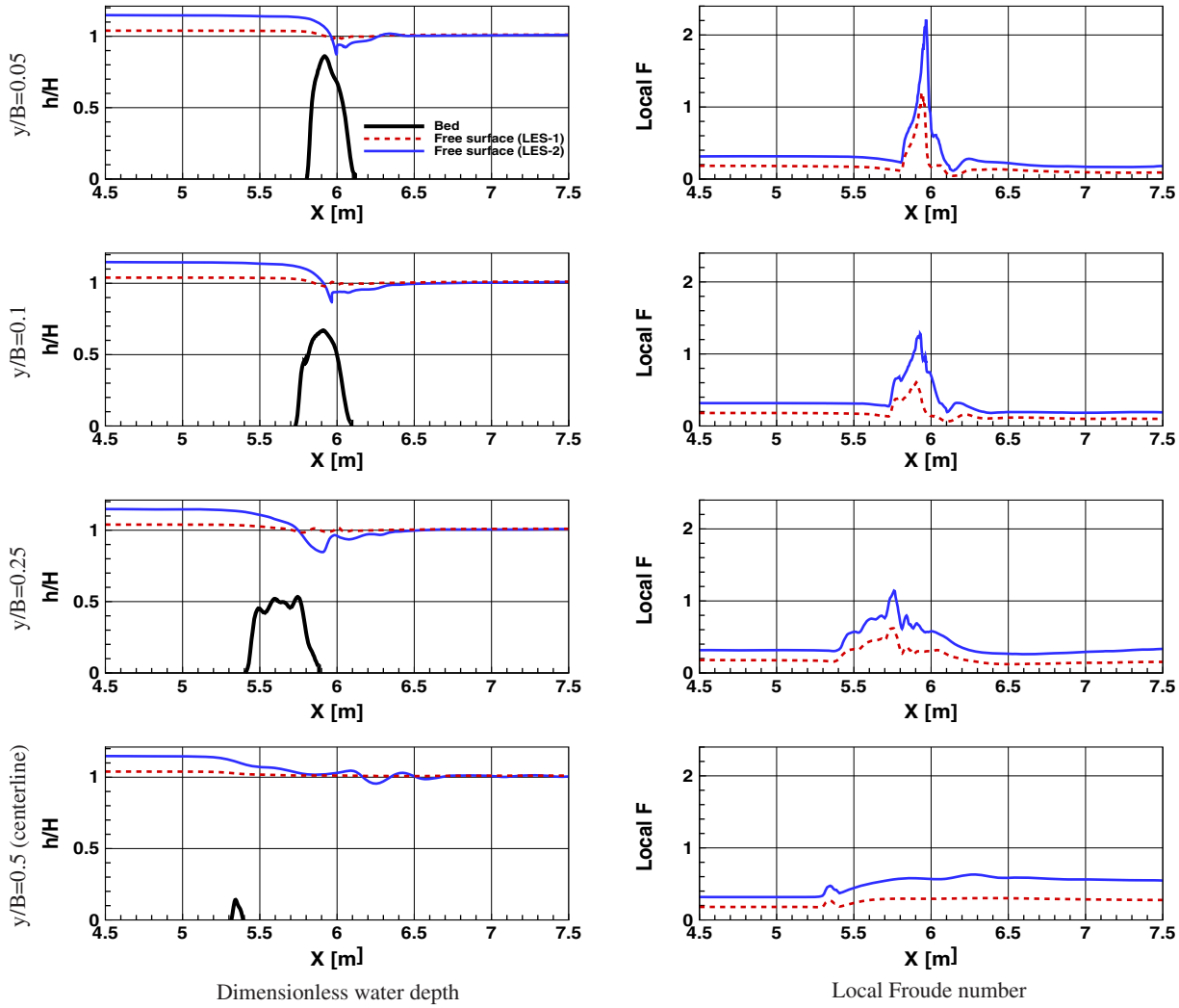

Fig. 11. Longitudinal profiles of the dimensionless time-averaged water depth and the local Froude number for LES-1 and LES-2

J. Hydraul. Eng. 2015.141.

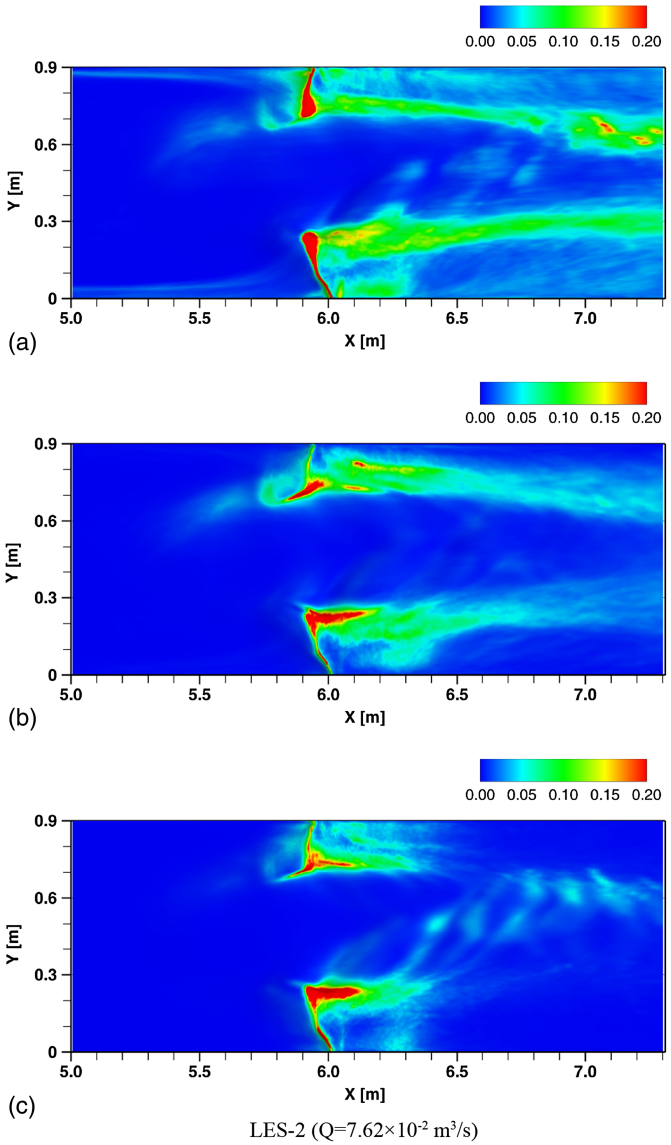

Fig. 12. Plan view of time-averaged velocity variances at the water surface nondimensionalized by U_0^2 (LES-2): (a) streamwise (x-direction); (b) spanwise (y-direction); and (c) vertical (z-direction) velocity variances

variance in these regions is much larger than that in the regions of shear layer. Fig. 12 shows that the hydraulic jump locally formed above the crest of the rock structure gives rise to the generation of intense velocity fluctuation, not just in the vertical direction but in the horizontal directions.

The simulation results in this section demonstrate the applicability of the coupled CURVIB–LES–level set model for solving real-life turbulent free surface flows past an arbitrarily complex structure with large free surface deformation. The computation shows that the higher discharge case gives rise to a nonnegligible free surface deformation and RMS fluctuation. Moreover, it is found that, in the shallow-depth regions, the hydraulic jump is formed and a high level of turbulence is generated. One can expect that the free surface deformation and the associated turbulence stresses could contribute significantly to the redistribution of the mean momentum. For instance, it is evident from the LES results that the variation of the mean water surface elevation (e.g., water ripples in LES-1; wavy water surfaces in LES-2) can cause remarkable changes in the mean streamwise velocity patterns at water surfaces. For instance, wavy water surfaces create alternating regions of high and low velocity [Figs. 6(a and b) and 10(a and b)]. The fact that the positions of the low- and high-velocity regions are approximately the same as those of the crests and troughs of the wavy water surfaces demonstrates that the water surface deformation driven by irregular structures/bathymetries in open channels could cause momentum redistribution at water surfaces. The momentum redistribution caused by water surface variations, however, cannot be accounted for in the LES with the free surface approximated as a rigid lid, which assumes a flat surface with the free-slip velocity condition and is often incorporated in low-Froude-number flow simulations.

Conclusions

In this paper, the LES of turbulent free surface flow involving arbitrarily complex structures is carried out using the CURVIB–LES–level set method. The method was applied to simulate flow past a cross-vane structure at two different discharge conditions—namely, LES-1 and LES-2. In LES-1, the comparison of the computation with the measurement showed satisfactory agreement. It is found that the LES could predict the time-averaged water surface elevation and the RMS fluctuation of water surface elevation with reasonable accuracy. The results of LES-2, on the other hand, showed that, at a higher discharge, the predicted flow field is significantly different from that of the low-discharge case, LES-1. Namely, the magnitude of the water surface deformation in the wake of the cross vane was much larger than that of LES-1. The maximum mean water surface displacement and the maximum RMS fluctuation were approximately 15 and 5% of the mean flow depth, respectively. It is also observed that the hydraulic jump occurring above the crest of the rock structure gives rise to a high level of turbulence intensity not only in the vertical direction but also in the horizontal directions.

Most of the previous studies on the numerical simulation of turbulent 3D free surface flows used the rigid-lid approximation, which assumes a flat free surface. The present results suggest that such approximation could lead to the loss of accuracy, especially when it is applied to high-Froude-number turbulent free surface flows. The displacement of the free surface location and the associated turbulence stresses may contribute significantly to the redistribution of the mean momentum at the water surface regions. In a future study, the numerical simulation with a rigid-lid assumption will be compared with the free surface resolving simulation to assess such effects.

Acknowledgments

This work was supported by National Science Foundation (NSF) grants EAR-0120914 (as part of the National Center for Earth-Surface Dynamics) and IIP-1318201. The first author acknowledges that this research was partially supported by a grant (14CTAP-C077529-01) from the Infrastructure and Transportation Technology Promotion Research Program funded by the Ministry of Land, Infrastructure and Transport of the Korean government.

References

Chachereau, Y., and Chanson, H. (2011). "Free-surface fluctuations and turbulence in hydraulic jumps." *Exp. Therm. Fluid Sci.*, 35(6), 896–909.
Ge, L., and Sotiropoulos, F. (2007). "A numerical method for solving the 3D unsteady incompressible Navier-Stokes equations in curvilinear

domains with complex immersed boundaries." *J. Comput. Phys.*, 225(2), 1782–1809.
Germano, M., Piomelli, U., Moin, P., and Cabot, W. H. (1991). "A dynamic subgrid-scale eddy viscosity model." *Phys. Fluids A*, 3(7), 1760–1765.
Hirt, C. W., and Nichols, B. D. (1981). "Volume of fluid (VOF) method for the dynamics of free boundaries." *J. Comput. Phys.*, 39(1), 201–225.
Hodges, B. R., and Street, R. L. (1999). "On simulation of turbulent nonlinear free-surface flows." *J. Comput. Phys.*, 151(2), 425–457.
Jiang, G.-S., and Shu, C.-W. (1996). "Efficient implementation of weighted ENO schemes." *J. Comput. Phys.*, 126(1), 202–228.
Kang, S., Borazjani, I., Colby, J. A., and Sotiropoulos, F. (2012). "Numerical simulation of 3D flow past a real-life marine hydrokinetic turbine." *Adv. Water Resour.*, 39, 33–43.
Kang, S., Lightbody, A., Hill, C., and Sotiropoulos, F. (2011). "High-resolution numerical simulation of turbulence in natural waterways." *Adv. Water Resour.*, 34(1), 98–113.
Kang, S., and Sotiropoulos, F. (2011). "Flow phenomena and mechanisms in a field-scale experimental meandering channel with a pool-riffle sequence: Insights gained via numerical simulation." *J. Geophys. Res.*, 116(F3), F03011.
Kang, S., and Sotiropoulos, F. (2012a). "Assessing the predictive capabilities of isotropic, eddy viscosity reynolds-averaged turbulence models in a natural-like meandering channel." *Water Resour. Res.*, 48(6), W06505.
Kang, S., and Sotiropoulos, F. (2012b). "Numerical modeling of 3D turbulent free surface flow in natural waterways." *Adv. Water Resour.*, 40, 23–36.
Kang, S., Yang, X., and Sotiropoulos, F. (2014). "On the onset of wake meandering for an axial flow turbine in a turbulent open channel flow." *J. Fluid Mech.*, 744, 376–403.
Kara, S., Stoesser, T., Sturm, T. W., and Mulahasan, S. (2014). "Flow dynamics through a submerged bridge opening with overtopping." *J. Hydraul. Res.*, 53(2), 186–195.
Khosronejad, A., Kang, S., Borazjani, I., and Sotiropoulos, F. (2011). "Curvilinear immersed boundary method for simulating coupled flow and bed morphodynamic interactions due to sediment transport phenomena." *Adv. Water Resour.*, 34(7), 829–843.
Khosronejad, A., Kang, S., and Sotiropoulos, F. (2012). "Experimental and computational investigation of local scour around bridge piers." *Adv. Water Resour.*, 37, 73–85.
Osher, S., and Fedkiw, R. (2002). *The level set method and dynamic implicit surfaces*, Springer, New York.
Osher, S., and Sethian, J. A. (1988). "Fronts propagating with curvature-dependent speed: Algorithms based on hamilton-jacobi formulations." *J. Comput. Phys.*, 79(1), 12–49.
Ramamurthy, A. S., Qu, J., and Vo, D. (2007). "Numerical and experimental study of dividing open-channel flows." *J. Hydraul. Eng.*, 10.1061/(ASCE)0733-9429(2007)133:10(1135), 1135–1144.
Rosgen, D. L. (2001). "The cross vane, W-weir and J-hook structures: Their description, design and application for stream stabilization and river restoration." *Proc., Wetland Engineering and River Restoration Conf. CD-ROM*, ASCE, Reston, VA.
Smagorinsky, J. S. (1963). "General circulation experiments with the primitive equations." *Mon. Weather Rev.*, 91(3), 99–164.
Sussman, M., and Fatemi, E. (1999). "An efficient, interface-preserving level set redistancing algorithm and its application to interfacial incompressible fluid flow." *SIAM J. Sci. Comput.*, 20(4), 1165–1191.
Sussman, M., Fatemi, E., Smereka, P., and Osher, S. (1998). "An improved level set method for incompressible two-phase flows." *Comput. Fluids*, 27(5–6), 663–680.
Sussman, M., Smereka, P., and Osher, S. (1994). "A level set approach for computing solutions to incompressible two-phase flow." *J. Comput. Phys.*, 114(1), 146–159.
Yang, X., Kang, S., and Sotiropoulos, F. (2012). "Computational study and modeling of turbine spacing effects in infinite aligned wind farms." *Phys. Fluids*, 24(11), 115107.
Yoon, T. H., and Kang, S.-K. (2004). "Finite volume model for two-dimensional shallow water flows on unstructured grids." *J. Hydraul. Eng.*, 10.1061/(ASCE)0733-9429(2004)130:7(678), 678–688.
Yue, W., Lin, C.-L., and Patel, V. C. (2005). "Large eddy simulation of turbulent open-channel flow with free surface simulated by level set method." *Phys. Fluids*, 17(2), 025108.